Characterization of Conductivity Changes During High-Frequency Irreversible Electroporation for Treatment Planning

Yajun Zhao, *Graduate Student Member, IEEE*, Suyashree Bhonsle, *Graduate Student Member, IEEE*, Shoulong Dong, *Student Member, IEEE*, Yanpeng Lv, Hongmei Liu, *Student Member, IEEE*, Ahmad Safaai-Jazi, *Senior Member, IEEE*, Rafael V. Davalos, *Member, IEEE*, and Chenguo Yao, *Member, IEEE*

***Abstract*—For irreversible-electroporation (IRE)-based therapies, the underlying electric field distribution in the target tissue is influenced by the electroporation-induced conductivity changes and is important for predicting the treatment zone. *Objective:* In this study, we characterized the liver tissue conductivity changes during high-frequency irreversible electroporation (H-FIRE) treatments of widths 5 and 10 μs and proposed a method for predicting the ablation zones. *Methods:* To achieve this, we created a finite-element model of the tissue treated with H-FIRE and IRE pulses based on experiments conducted in an *in-vivo* rabbit liver study. We performed a parametric sweep on a Heaviside function that captured the tissue conductivity versus electric field behavior to yield a model current close to the experimental current during the first burst/pulse. A temperature module was added to account for the current increase in subsequent bursts/pulses. The evolution of the electric field at the end of the treatment was overlaid on the experimental ablation zones determined from hematoxylin and eosin staining to find the field thresholds of ablation. *Results:* Dynamic conductivity curves that provided a statistically significant relation between the model and experimental results were determined for H-FIRE. In addition, the field thresholds of ablation were obtained for the tested H-FIRE parameters. *Conclusion:* The proposed numerical model can simulate the electroporation process during H-FIRE. *Significance:* The treatment planning method developed in this study can be translated to H-FIRE treatments of different widths and for different tissue types.**

***Index Terms*—High Frequency bipolar pulses, electrochemotherapy, tumor ablation, nonthermal focal therapy, cancer treatment.**

I. Introduction

When exposed to externally applied, pulsed electric fields (PEFs), the biological cell experiences an increase in its transmembrane potential (TMP). If the PEFs intensity is high enough, the TMP reaches a threshold that causes the induction of nanoscale defects in the plasma membrane. This phenomenon, known as electroporation, is utilized in medical technologies such as electrochemotherapy (ECT) [1]–[4] and irreversible electroporation (IRE) [5]–[9] to treat tumors. During ECT treatment, parameters are chosen such that electroporation is temporary, allowing the delivery of macroscale drugs, which could not permeate the cell membrane prior to application of the PEF. Alternately, IRE employs parameters that result in cell death due to the loss of cell homeostasis caused by the nanoscale defects (reversible and/or irreversible) [10], while also limiting the amount of thermal damage to the tissue.

Typically, thermal ablation techniques such as microwave, radio frequency (RF) and focused ultrasound that work by increasing the temperature in a target area to a critical threshold to destroy a mass of tissue [11]. Conversely, IRE's mechanism of cell death is predominantly non-thermal, and therefore, the treatment modality is often referred to as non-thermal ablation. The advantage of such a non-thermal technique of tumor treatment is that the ablation outcome is not affected by blood perfusion and heat sensitive critical structures such as blood vessels near the treatment zone can be spared. These characteristics have enabled the widespread use of IRE in the clinical environment to treat tumors in organs such as the liver [12], kidney [13], and pancreas [14], [15].

IRE treatments are generally performed with needle electrodes placed in or around the target tumor tissue. The applied pulses induce an electric field distribution in the target area.

Manuscript received August 19, 2017; revised November 15, 2017; accepted November 24, 2017. Date of publication November 28, 2017; date of current version July 17, 2018. This work was supported in part by the National Natural Science Foundation of China (51321063), in part by the Natural Science Foundation Project of CQ CSTC (cstc2014jcyjjq90001), in part by the Fundamental Research Funds for the Central Universities (No.106112017CDJQJ158835), in part by the Pancan under the Award 6-65-IANN, in part by the NSF IIP under the Award 1346343, and in part by the NSF CIT STTR under the Award 14S-003-LS. *(Corresponding author: Chenguo Yao.)*

Y. Zhao, S. Dong, Y. Lv, and H. Liu are with the State Key Laboratory of Power Transmission Equipment and System Security and New Technology, School of Electrical Engineering, Chongqing University.

S. Bhonsle and A. Safaai-Jazi are with the Department of Electrical and Computer Engineering, Virginia Tech.

R. V. Davalos is with the Department of Biomedical Engineering and Mechanics, Virginia Tech.

C. Yao is with the State Key Laboratory of Power Transmission Equipment and System Security and New Technology, School of Electrical Engineering, Chongqing University, Chongqing 400044, China (e-mail: yaochenguo@cqu.edu.edu).

Digital Object Identifier 10.1109/TBME.2017.2778101

Depending upon the pulse parameters and tissue-type, the local electric field determines if electroporation is reversible, irreversible, or if thermal damage has occurred. To maintain its non-thermal mode of operation, IRE treatment utilizes 50 to 200 unipolar pulses of widths between 50 μs and 100 μs, pulse repetition rates of $\sim$1 Hz, and voltage-to-distance ratios of 1500 to 3000 V/cm (applied voltage/electrode spacing) [16]–[18]. More recently, a second-generation IRE system called high frequency irreversible electroporation (H-FIRE) was proposed. H-FIRE utilizes bipolar pulses of widths from 0.5 μs to 10 μs that provide additional benefits over the long unipolar pulses [19]. The narrow bipolar H-FIRE pulses have nerve stimulation thresholds much higher than IRE pulses, and therefore, obviate the need for neuroparalytics that are required during IRE treatment to suppress muscle contractions [19], [20]. In the absence of neuroblockers during conventional IRE, muscle contractions are shown to be severe enough to not only cause pain, but also displace electrodes, consequently affecting the ablation characteristics [18]. Another benefit of H-FIRE is associated with the tissue's dielectric response to the high frequency content of pulses (versus the lower frequency IRE pulses), which is less influenced by electroporation related changes and more uniform across different tissues, making the outcome of the treatment planning more accurate [21]–[23]. To retain the benefits of non-thermal IRE, the on-time of the H-FIRE bursts is set to 100 μs, and the burst frequency is set to 1 Hz. According to the existing studies [24]–[26], to get an appropriate lethal volume H-FIRE treatments often utilize 80 to 300 bursts at voltage-to-distance ratios of 1500 to 3000 V/cm.

Pre-treatment planning algorithms that predict the field distribution in tissue, and consequently, the ablation zone are critical to the success of IRE and H-FIRE therapy. An important component of such algorithms is the dynamic change in conductivity of a given tissue in response to electroporation pulses that influences the field distribution [27], [28]. The field distribution, along with the electric field threshold of ablation (i.e., the field contour that traces the ablation zone), can be used to predict the ablation zone. While several studies have investigated the redistribution of the electric field during IRE treatment, due to such non-linear changes in conductivity [29], [30], the dynamic changes in tissue properties during H-FIRE treatment are yet to be studied in biological tissue in vivo.

In the present study, we have characterized the dynamic changes in tissue electrical properties during H-FIRE treatment, consisting of 5 μs and 10 μs bursts of on-time 100 μs, on in vivo rabbit livers. In addition, for comparison, we have quantified the tissue properties using traditional IRE treatment, consisting of 100 μs pulses. Models that incorporated these quantified tissue properties were then employed to determine the electric field threshold of ablation for the tested parameters.

Specifically, to achieve this goal, a finite element model of the electric field behavior in tissue during H-FIRE and IRE treatment using two-needle electrodes was simulated to examine the redistribution of the field due to electroporation and temperature effects. The Heaviside curve, adapted from prior studies [30], was used to describe the dynamic change in the tissue conductivity as a function of the local electric field. The parameters in this function were optimized by yielding a model current close to the measured current obtained from in vivo H-FIRE experiments on rabbit livers at the end of the first burst or pulse. Prior studies show that while the current increase in the first pulse is mainly due to electroporation effects; temperature effects dominate the differential increase in current in the subsequent pulses [29]. Therefore, a temperature module that reflected the cumulative effect of the multiple pulses was added to model the conductivity increase due to temperature and predict the electric field distribution at the end of the treatment. Finally, the electric field contour (from the end of the treatment) that best predicted the outer edges of the boundary was selected as the electric field threshold of ablation for the tested parameters.

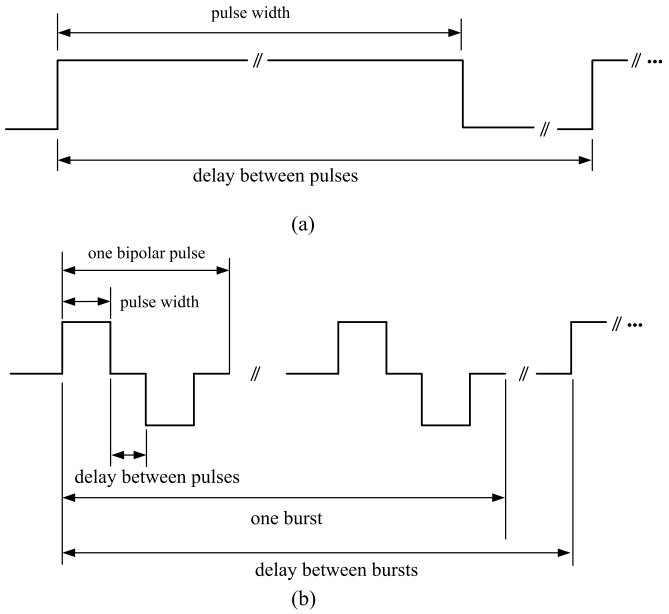

Fig. 1. Schematic of an IRE. (a) Pulse and H-FIRE burst (b).

II. Material and Methods

A. Pulse Parameters and Experimental Setup

IRE and H-FIRE treatments were conducted on *in vivo* rabbit livers in a prior study [25]. The schematic of an IRE pulse and H-FIRE burst are shown in Fig. 1, and the treatment parameters are described in Table I. The output voltage and currents were measured using a WavePro 760Zi-A oscilloscope (Teledyne LeCroy Inc., New York, USA) with a PPE-5kV high voltage probe (Teledyne LeCroy Inc., New York, USA) and a Pearson current probe 6600 (Pearson Electronics Inc., Palo Alto, USA).

The liver samples were harvested 72 hours after treatment. The samples were stained using Hematoxylin and Eosin (H&E). Images of each tissue section were acquired using an Aperio LV1 Digital Pathology Slide Scanner (Leica Biosystems Inc., Buffalo Grove, USA). The middle plane of the ablation zone perpendicular to the electrodes was selected to represent the ablation sizes (length and width). The ablation zones were marked and measured by professional pathologists. The details of these can be found in our previous study [25].

TABLE I
PULSE PARAMETERS FOR H-FIRE AND IRE IN THE EXPERIMENTS

Pulse Type	Pulse Width (μs)	Applied Voltage (V)	Output Voltage (V)	Bipolar pulses per burst	Inter-pulse /burst delay (s)	Pulse/burst number
H-FIRE	5-2-5*	1000	913.04 ± 5.99	10	1	90
	5-2-5	1250	1136.70 ± 3.14	10	1	90
	5-2-5	1500	1380.39 ± 9.04	10	1	90
	5-2-5	1750	1607.41 ± 2.22	10	1	90
	5-2-5	2000	1830.62 ± 6.20	10	1	90
	10-2-10	1000	906.18 ± 0.54	5	1	90
	10-2-10	1250	1135.99 ± 2.51	5	1	90
	10-2-10	1500	1390.31 ± 16.55	5	1	90
	10-2-10	1750	1583.54 ± 5.08	5	1	90
	10-2-10	2000	1838.26 ± 9.87	5	1	90
IRE	100	800	780.13 ± 7.36	–	1	90
	100	1000	973.79 ± 4.33	–	1	90
	100	1250	1209.33 ± 5.62	–	1	90
	100	1500	1454.58 ± 7.87	–	1	90

*5-2-5 means positive pulse width-inter-pulse delay-negative pulse width.

B. Numerical Model – Single Pulse/Burst

Similar to prior studies [27], a block geometry of the dimensions 3.2 × 3.2 × 1.7 cm with liver tissue properties was used for simulating the electric field distribution in the experimental tissue at the end of the first pulse/burst. The numerical model was solved using a commercial finite element package (Comsol Multiphysics, v.5.2; Stockholm, Sweden). The electrode configuration/material consisted of two stainless steel cylinders with a diameter of 1mm, a separation of 1cm and an exposure length of 8 mm, to mimic the actual experimental setup. The governing equation for the electric potential evolution solved under the electro-quasistatic approximation [22] is given in (1). The electric field distribution was obtained by taking the gradient of the electric potential as given in (2).

$$\nabla \cdot (\sigma \nabla \varphi) + \varepsilon_0 \varepsilon_r \nabla \cdot \left(\frac{\partial \nabla \varphi}{\partial t} \right) = 0 \tag{1}$$

$$\bar{E} = -\nabla \varphi \tag{2}$$

Here, σ is the tissue conductivity, φ the electric potential, ε_r is the relative permittivity of the tissue, and ε_0 is the permittivity of free space. The electrical boundary conditions in contact with the source and the sink electrodes were set to $\varphi = \mathrm{V(t)}$ and $\varphi = 0$, respectively. Here, V(t) is an IRE pulse or H-FIRE burst constructed by using combinations of smoothed Heaviside functions and multiplied by pulse amplitude. Specifically for an IRE pulse, two Heaviside functions with a 100 μs delay (pulse width) and rise/fall time of 50 ns were used to construct a unipolar pulse. For the H-FIRE burst, four Heaviside functions (rise/fall times of 50 ns) with time delays corresponding to the widths and inter-phase delay were used to create one bipolar pulse. The bipolar pulse was then extended to a periodic function to obtain one bipolar pulse burst of on-time 100 μs. All pulses/bursts were tested at the average output pulse amplitudes given in Table I. The normal current density over one of the electrode surfaces was integrated to calculate the total current delivered to the tissue. All remaining boundaries were treated as electrically insulating. The mesh size was refined until there was less than a 2% difference in the field results between refinements, resulting in fine mesh setting.

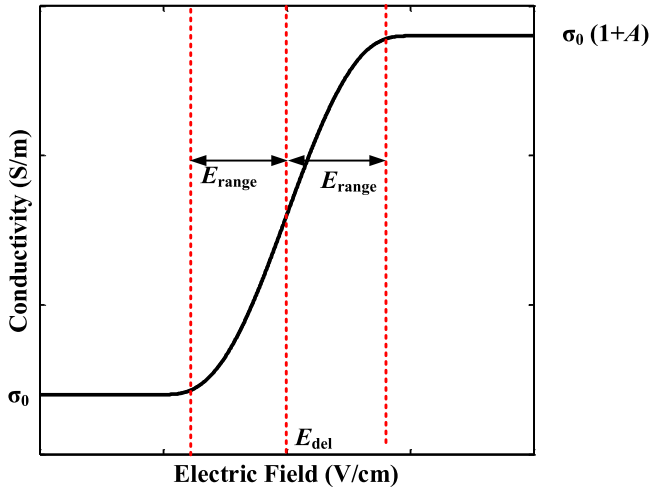

Fig. 2. Schematic of conductivity versus the electric field curve from (3). Here, σ_0 is the initial conductivity of the tissue and $\sigma_0(1+A)$ is the maximum tissue conductivity after electroporation. E_{del} is the middle point of the transition zone and E_{range} gives half the value of the transition zone that traverses from $E_{\mathrm{del}} - E_{\mathrm{range}}$ to $E_{\mathrm{del}} + E_{\mathrm{range}}$.

For the first pulse/burst, the tissue conductivity was treated as dynamically changing with the electric field (electroporation-related effects) alone and is given in (3).

$$\sigma\left(\left|\bar{E}\right|\right) = \sigma_0 \left(1 + A flc2hs\left(\left|\bar{E}\right| - E_{\mathrm{del}}, E_{\mathrm{range}}\right)\right) \tag{3}$$

Here, σ_0, the initial conductivity of tissue (i.e., prior to treatment), was fixed to a certain value and $|\bar{\mathrm{E}}|$ is the underlying magnitude of the electric field. The *flc2hs* is a smoothed Heaviside function with a continuous second derivative that ensures convergence of numerical solution. In the given form, the function $\sigma(|\bar{\mathrm{E}}|)$ changes from σ_0 to $\sigma_0(1+A)$ over the range $2E_{\mathrm{range}}$ with transition starting at $E_{\mathrm{del}} - E_{\mathrm{range}}$ and ending at $E_{\mathrm{del}} + E_{\mathrm{range}}$ (Fig. 2). Therefore, E_{del} is the mid-point of the transition zone and E_{range} gives half the value of the transition zone. The

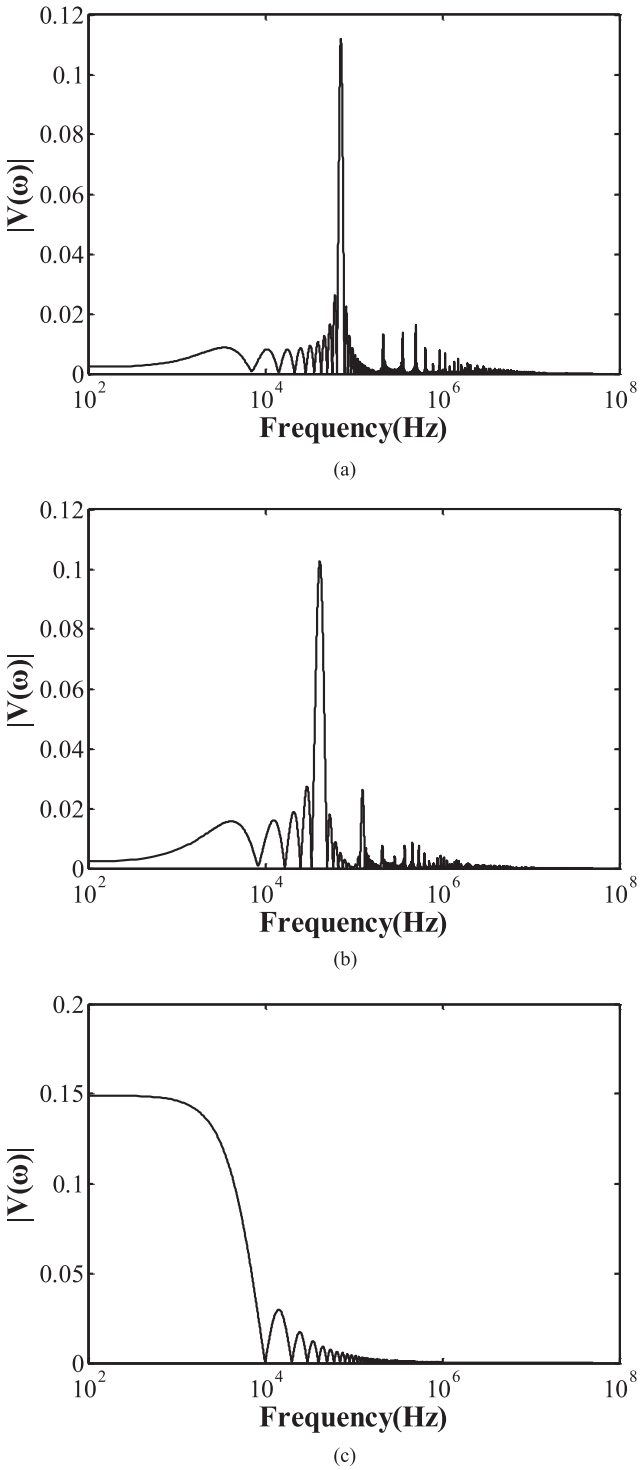

Fig. 3. The Fourier spectrum of the first burst of the H-FIRE voltage waveform consisting of bipolar pulses of schemes 5-2-5 μs and (a) 10-2-10 μs (b) applied at a voltage of 1500V. The Fourier spectrum of the first 100 μs IRE pulse applied at a voltage of 1500 (c).

coefficient A allows the function to account for different degrees of change for different pulse widths.

The parameters A, E_{del}, and E_{range} were treated as unknowns, and were optimized using the parametric sweep module to make the modeled current close to the experimental current.

TABLE II
THE CONDUCTIVITY AND PERMITTIVITY FOR DIFFERENT PULES

Pulse width (μs)	Frequency (kHz)	Conductivity (S/m)	Relative permittivity	References
5	71.4	0.23	8873.8	[25], [32]
10	41.7	0.21	11823	[25], [32]
100	5	0.12	42672	[25], [32]

TABLE III
PARAMETER RANGES TESTED IN THE MODEL

Parameter	Range	Unit	References
A	0-3	–	[24]–[26], [30], [31]
E_{del}	0–3000	V/cm	[22], [32]
E_{range}	0–E_{del}	V/cm	–

For the simulation, the initial conductivities and permittivities were obtained from the literature [31], [32]. Biological tissue exhibits frequency-dependent conductivity and permittivity behavior [31]. To determine the electrical properties at the constituent frequencies of the pulse/burst, first, the frequency spectrum of the IRE pulse and H-FIRE burst was determined using the fast Fourier transform (fft) function in Matlab (Mathworks Inc., Natick, MA, US). The pulses were saved at a sample frequency of 100 MHz and zeros were appended to the signal to achieve a frequency resolution of 100 Hz. The rise time of the recorded pulses was between 30–60 ns and affected frequency contents above ~1 MHz. This was verified by testing H-FIRE bursts of different rise times (data not shown here). Next, the values of the initial conductivity were chosen at frequencies at which the magnitude of the input voltage in the Fourier spectrum was maximized (Fig. 3). For IRE pulses, though frequencies up to 10 kHz exhibit the same amplitude weight in the spectrum, the electrical properties did not significantly differ between 1 Hz and 10 kHz and therefore, the electrical properties were chosen at a frequency of 5 kHz. For H-FIRE pulses, the electrical properties were chosen at 41.7 kHz and 71.4 kHz for the 10 μs and 5 μs pulses, respectively. Table II shows the values of the conductivities and permittivities at the chosen frequencies.

C. Parameter Estimation

Table III shows the ranges over which the variables A, E_{del}, and E_{range} were scanned to obtain an optimal fit between the model and experimental current. The experimental current during the last 1 μs of the first pulse/burst was averaged to reduce the effects of noise. According to previous studies [27], [29], [30], [33], [34], the maximum conductivity change due to permeabilization was expected to be, at most, 4 times that of the initial conductivity and therefore, the parameter A was tested between 0 and 3. Next, the parameter E_{del}, which determines the midpoint of the transition zone of the Heaviside function, was tested over the range of 0 to 3000 V/cm. Prior studies have found that E_{del} for traditional 100 μs pulses is ~600 V/cm [30]. However, this value was expected to be higher for 5 μs and 10 μs pulses,

as their permeabilization thresholds are ∼1.5 – 3 times higher (depending on pulse width) [19] than the 100 μs pulses and therefore, E_{del} was tested over a larger range. Finally, E_{range}, which controls the transition range of the Heaviside function around E_{del}, was tested between 0 and E_{del} V/cm. Since, the low side of the transition zone, $E_{\mathrm{del}} - E_{\mathrm{range}}$, is always positive, E_{range} is always less than E_{del}.

$$\mathrm{TIC} = \frac{\sqrt{\Sigma_i (I_i - I_{mi})}}{\sqrt{\Sigma_i I_i^2} + \sqrt{\Sigma_i I_{mi}^2}} \tag{4}$$

Theil's inequality criteria (TIC), given in (4), was used for determining the set of parameters that resulted in the best match between the model and experimental current for all amplitudes. I_i is the experimental current and I_{mi} is the modeled current, for the ith experiment. One TIC value was obtained for each pulse/burst type i.e., a 100 μs pulse, a 5-2-5 μs burst and a 10-2-10 μs burst. More details of this test can be found in [27]. The values of TIC are in the range of 0 and 1, where values below 0.3 indicate good agreement; therefore, the conductivity function parameters that resulted in the lowest TIC for the currents were selected.

In addition to this test, a coefficient of determination, R^2 defined in (5) was calculated to provide a statistical measure of how well the optimized model data approximates the experimental data, for each pulse/burst type [34].

$$\begin{aligned} R^2 &= 1 - \frac{SS_{res}}{SS_{tot}} \\ SS_{res} &= \sum_i (I_i - I_{opti})^2 \\ SS_{tot} &= \sum_i (I_i - \bar{I})^2 \end{aligned} \tag{5}$$

Here, I_i is the experimental current, $\bar{I}$ is the average of the experimental currents and I_{opti} is the optimized model current for each pulse amplitude. The coefficient R^2 takes on values between 0 and 1, where higher values indicate a good fit between the optimized model and experimental data.

D. Multi-Pulse Temperature Effects

Initial studies characterizing the conductivity changes discounted the effects of multiple pulses on the tissue, i.e., they assumed each consecutive electroporation-inducing pulse produced the same current or conductivity and therefore, the same electric field distribution [27], [35]. However, experimentally it was observed that consecutive pulses produced higher current/conductivity than the previous pulse [29]. These could be attributed to long-term pores, re-sealing dynamics, changes in tissue structure and temperature effects. A study on kidney tissue [29], however, showed that for IRE pulse protocols consisting of 200 pulses, the differential increase in conductivity between consecutive pulses is dominated by temperature increase. Based on this assumption, the conductivity at the end of each consecutive pulse was modeled as a function of temperature in addition to the electric field magnitude in the given (6).

$$\begin{aligned} \sigma(|\bar{E}|, T) &= \sigma(|\bar{E}|) + \sigma(T) \\ &= \sigma_0 [1 + Aflc2hs\left(|\bar{E}| - E_{\mathrm{del}}, E_{\mathrm{range}}\right) \\ &\quad + \alpha (T - T_0)] \end{aligned} \tag{6}$$

Here, T_0 is the ambient temperature before the treatment and was set to physiologic tissue temperature of 310.15K (37 °C). T is the tissue temperature, and α is the temperature coefficient that reflects the tissue conductivity change with temperature. For liver tissue, prior studies have determined the value of α to be 2%/K [36].

The instantaneous temperature distribution (T) was determined using the Pennes' Bioheat equation (7) [29].

$$\nabla \cdot (k \nabla T) + \rho_b \omega_b c_b (T_a - T) + q''' + \frac{\sigma |\nabla \Phi|^2 \cdot d}{\tau} = \rho c_p \frac{\partial T}{\partial t} \tag{7}$$

Here, k is the thermal conductivity of the tissue, c_b and c_p are the blood and tissue heat capacity, respectively, T_a is the arterial temperature, ρ_{b} and ρ are the blood and tissue density, q''' is the metabolic heat generation, ω_{b} is the blood perfusion rate, and $\sigma|\nabla\Phi|^2$ is the Joule heating term that accounts for resistive heating of the tissue.

As proposed in prior studies [29], to simplify the simulation process, the Joule heating term was scaled according to the pulse or burst on-time, d, divided by the period between the pulses or bursts τ, averaging the heating over the entire intra- and inter-pulse duration. The parameters used in the Pennes' Bioheat equation are shown in Table IV.

TABLE IV
PHYSICAL PROPERTIES USED FOR COMPUTATIONAL MODELING

Parameter	Value	Unit	Reference
ρ, density	1079	kg/m^3	[36]
ρ_b, blood density	1060	kg/m^3	[30]
c_p, heat capacity	3540	J/kg/K	[36]
k, thermal conductivity	0.52	W/m/K	[36]
w_b blood perfusion term	7.15×10^{-3}	1/s	[30]
c_b, heat capacity of blood	3840	J/kg/K	[30]
T_a, arterial temperature	37	°C	[36]
q' metabolic heat production	33800	W/m^3	[36]

E. Electric Field Thresholds of Ablation

To validate the multi-pulse numerical model as well as determine the electric field threshold of ablation for the different IRE and H-FIRE pulse parameters (Table I), the electric field contours that were obtained at the end of the simulation were matched to the ablation zone. Specifically, the mid-plane contour that best mapped the outer edges of the ablation zone was selected as the electric field threshold of ablation (E_{th}) and used for further analysis. The long and short axis of this contour was measured using ImageJ (National Institutes of Health, Bethesda, Maryland) and independent t-tests were performed in Excel (Microsoft Corporation, Redmond, WA) between these

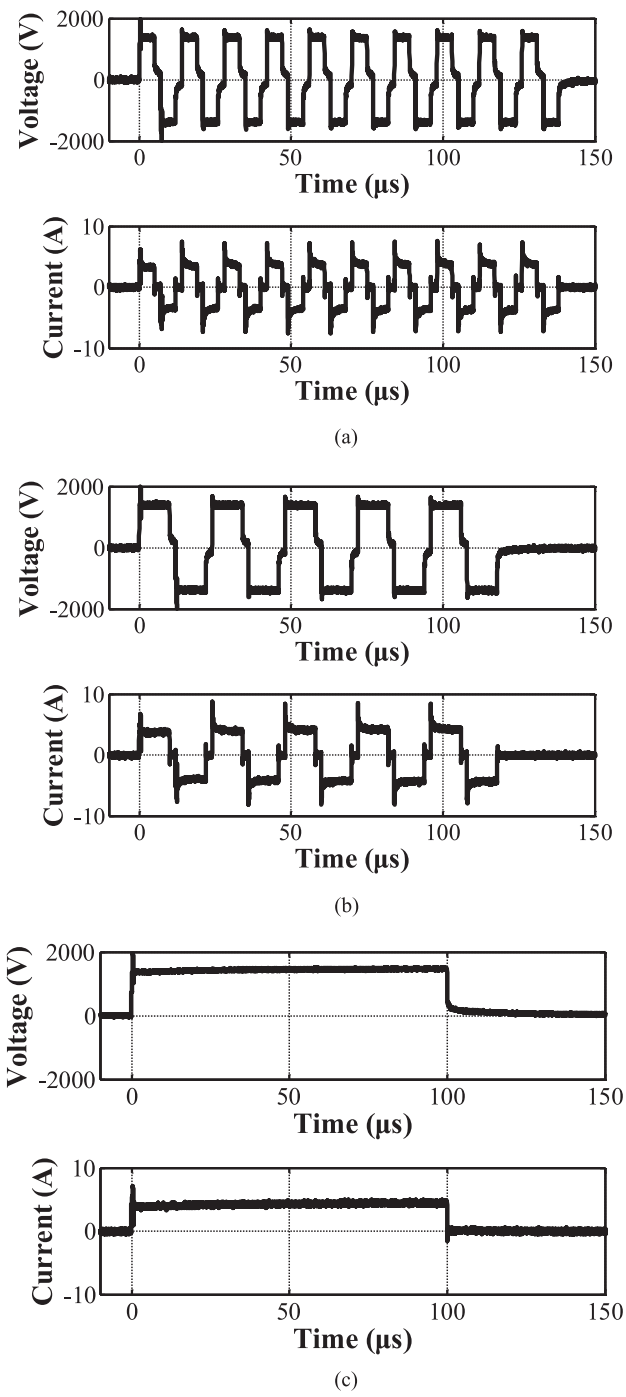

Fig. 4. The recorded first pulse/burst of voltage and current of H-FIRE with pulse width of (a) 5 μs, (b) 10 μs and (c) conventional IRE pulse. The amplitude in the waveform shown here was 1500V, the inter pulse delay for H-FIRE is 2 μs and the rise time of all pulses is about 30–60 ns.

values and those of the actual ablations. A difference with $P \leq 0.05$ was considered statistically significant.

III. Results and Discussion

A. Estimation of the Parameters

The experimental voltage and current during the first H-FIRE burst for the 5 μs and 10 μs pulses is shown in Fig. 4(a) and Fig. 4(b), respectively, and the first IRE pulse is shown in Fig. 4(c). The parameters in the conductivity function were optimized to make the simulation current close to the experimental current at the end of the first burst or pulse (flat portion) and are shown in Table V. The conductivity curves plotted from the optimized parameters are shown in Fig. 5. This curve quantifies the change in conductivity as a function of the electric field (due to electroporation, σ(E)). While this curve is determined from the first pulse (assuming negligible temperature effects), it is assumed that consecutive pulses also show similar change in conductivity due to electroporation (applied electric field). The additional increase in current/conductivity in the consecutive pulses is due to temperature (σ(T)). Therefore, the change in conductivity during each consecutive pulse can be determined from σ(E) + σ(T) [29].

It was found that E_{del}, which determines the electric field magnitude at the mid-point of the transition zone of Heaviside function, is lower for the IRE pulse than the H-FIRE burst. In addition, E_{range}, which determines transition zone of the Heaviside function around E_{del}, was found to be higher for the H-FIRE burst.

Next, it was observed that the parameter, A, which indicates the extent of conductivity change during the first pulse or burst was higher for the IRE pulse than the H-FIRE burst. This result can be attributed to pore dynamics that come into play during the application of electroporation-inducing pulses. Studies have shown that the size and number of pores created during the delivery of longer, unipolar pulses is greater than shorter, bipolar pulses, thereby, causing a larger increase in permeability [37], [38] and consequently, the electrical conductivity. Similar to prior studies [21], this result shows that the conductivity

TABLE V
The Parameters in the Model of Conducvtivity

Pulse Width (μs)	E_{del} (V/cm)	E_{range} (V/cm)	A
5	1200	350	0.9
10	1150	300	1.05
100	700	150	1.8

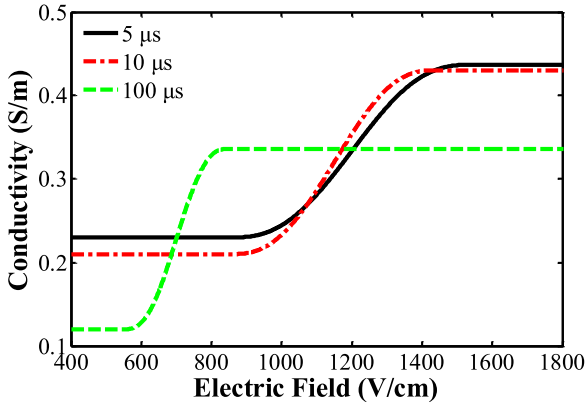

Fig. 5. Conductivity dependency on electric field for conventional IRE (green dashed line) and H-FIRE with pulse width of 5 μs (black solid line) and 10 μs (red double dashed line).

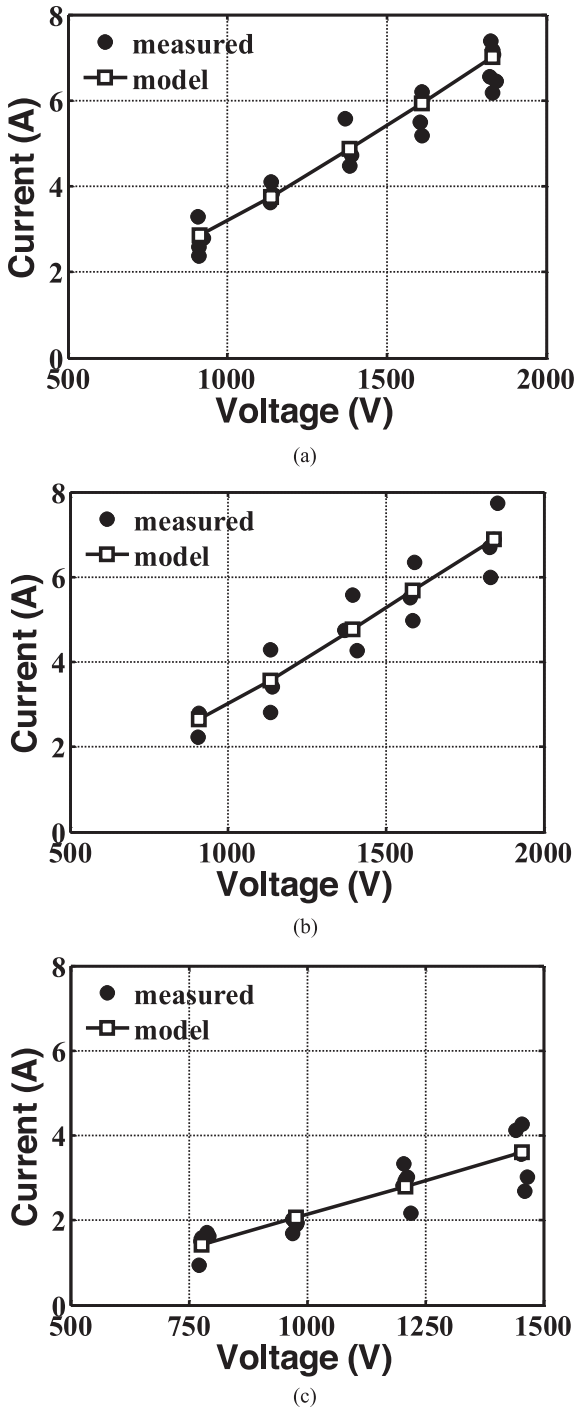

Fig. 6. Comparison of the modeled current (hollow squire connected by solid line) and experimental current (black dots) at the end of the first pulse or burst with H-FIRE pulse widths of 5 μs (TIC = 0.041, $R^2 = 0.929$) (a), and 10 μs (TIC = 0.053, $R^2 = 0.892$) (b) and conventional 100 μs IRE pulse (TIC = 0.079, $R^2 = 0.799$) (c).

changes during treatment with H-FIRE pulses are mitigated. Additionally, the conductivity changes are reduced with decreasing widths, i.e., the value of parameter *A* is smaller for the 5 μs pulses than the 10 μs pulses.

The modeled and the measured currents at the end of the first pulse/burst for different applied voltages are shown in Fig. 6. The chosen parameters of the conductivity curves resulted in TIC values of 0.041, 0.053 and 0.079 for 5 μs, 10 μs and 100 μs pulses, respectively. In addition, the coefficients of determination R^2 were 0.929, 0.892 and 0.799 for 5 μs, 10 μs and 100 μs pulses, respectively. These values show that there was good agreement between the simulation and experimental results.

Overall, it was found that our method of determining optimal parameters between the modeled and measured currents resulted in better fits for the H-FIRE bursts than the IRE pulse. This could be attributed to larger variability in the measured current results during IRE treatment. This inconsistency could be attributed to the movement of the electrodes due to presence of muscle contractions during IRE treatment [25]. During H-FIRE experiments, the muscle contractions were significantly suppressed, leading to results that are more consistent.

B. Validation by Ablation Size

The representative images for the electric field threshold contour overlaid on the ablation zones for the 5 μs, 10 μs and 100 μs pulses with a pulse amplitude of 1250V are shown in Fig. 7(a), Fig. 7(c) and Fig. 7(e), respectively. Fig. 7(b), Fig. 7(d) and Fig. 7(f) are the partial enlarged view of live/dead regions. For the 90 pulse/burst treatment, the electric field thresholds that best determined the ablation zones were found to be 713 V/cm, 610 V/cm and 450 V/cm for the 5 μs, 10 μs and 100 μs pulses, respectively. Similar to prior studies [17], [19], it was found that for the same on-time, the ablation sizes were larger and the ablation thresholds were smaller for the longer pulses.

Prior studies have shown that, for an 8 pulse protocol, the inflection points ($E_{\mathrm{del}} - E_{\mathrm{range}}$ and $E_{\mathrm{del}} + E_{\mathrm{range}}$) on the conductivity curves are an indication of the reversible and irreversible electric field thresholds of permeabilization [27]. Based on this, the thresholds for irreversible electroporation were 1550 V/cm, 1450 V/cm and 850 V/cm for the 5 μs, 10 μs and 100 μs pulses, respectively. The results, therefore, indicate that the irreversible ablation thresholds for the 90 IRE pulse treatment were smaller than the reported ablation thresholds for the 8 pulse treatment. This trend between the pulse number and ablation size is in agreement with the current literature [17], [39], however, the exact relation between pulse number and ablation thresholds is yet to be determined and is proposed as a future study.

Table VI shows the measurements of the long and short axes of the ablation zones determined from the experiments [25], the simulations, and the results of the independent t-tests. Of the 28 comparisons, only two comparisons between the simulated and actual ablation zones showed statistical differences. These were a *P*-value of 0.0390 for the long axis of an ablation obtained from the 10 μs burst treatment of 2000V amplitude and a *P*-value of 0.0166 for the long axis of an ablation obtained from the 100 μs pulse treatment of 1250V amplitude.

Some limitations of this study need to be addressed in future work. The conductivity changes quantified in this study were attributed to short-term pores created during the pulse/burst and temperature increase during treatment; however, the effects of long-term pores present during the inter-pulse or burst delay

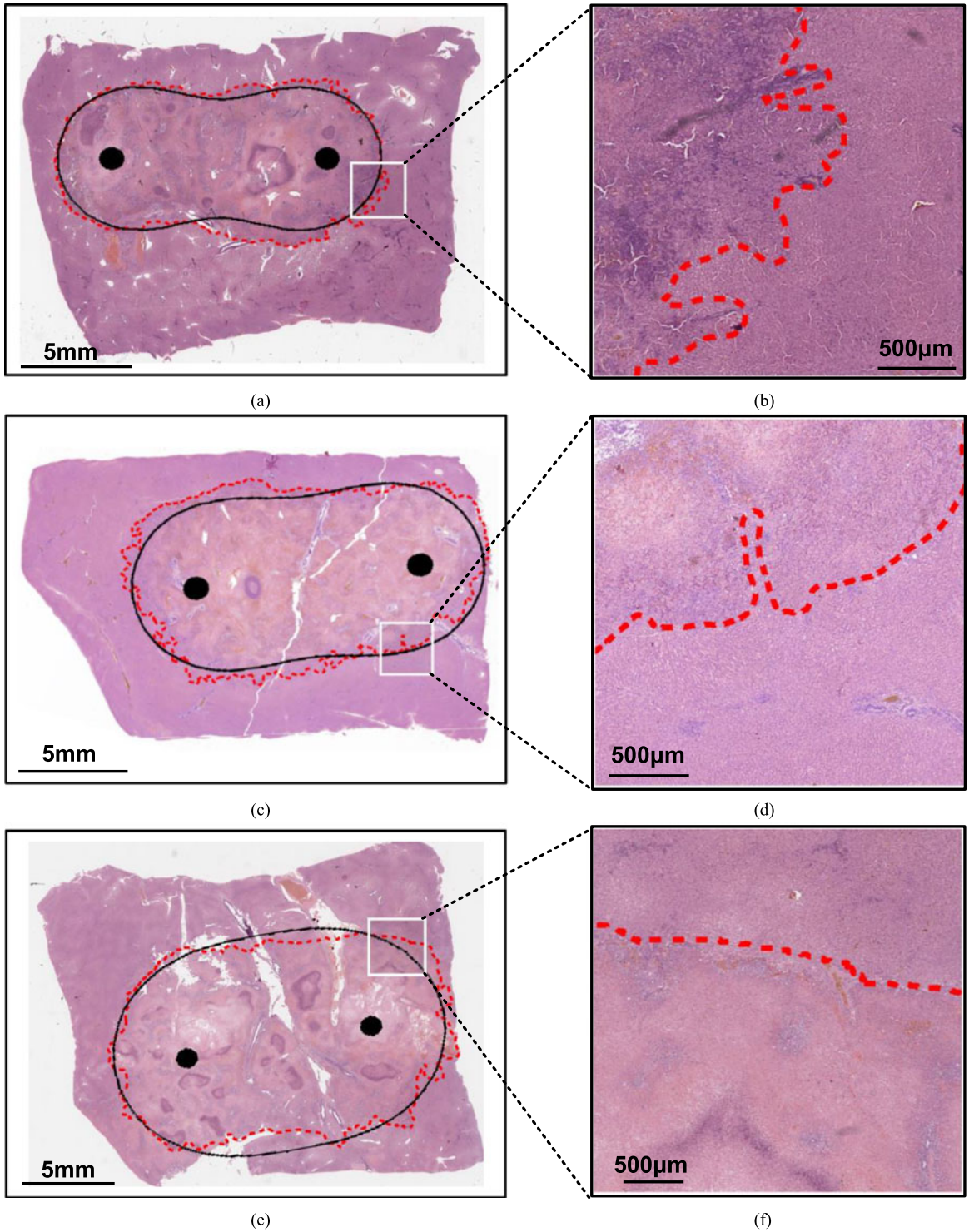

Fig. 7. The ablation zones (red dash lines in a, c, e) and the electric field thresholds of ablation (black solid lines in a, c, e) for pulses of amplitude 1250V. For 5 μs, the threshold is 713 V/cm (a) and the margin is clearly shown in (b). For 10 μs, the threshold is 610 V/cm (c) and the margin is clearly shown in (d). For 100 μs, the threshold is 450 V/cm (e) and the margin is clearly shown in (f).

were ignored. In current literature, only one study has explored the effects of the resealing dynamics on tissue conductivity for a short number of pulses (8 pulses) [40]. However, the model employs a large number of empirically parameters, which are difficult to translate to 80–100 pulse protocols. Next, while the tissue properties were characterized using healthy rabbit livers, the differences in these electrical properties for tumor tissue and across different species is yet to be studied.

TABLE VI
SIZE OF THE ABLASION ZONES AND THE ELECTRIC FIELD ISOLINE

Pulse Width (μs)	Amplitude (V)	Long Axis (mm)		P value	Short Axis (mm)		P value	Sample Size N
		Experiment	Model		Experiment	Model		
5	1000	13.44 ± 1.00	13.97	0.4435	6.28 ± 0.35	5.74	0.0514	5
5	1250	14.16 ± 0.62	14.9	0.2026	8.62 ± 1.33	6.51	0.1245	3
5	1500	17.16 ± 0.48	15.75	0.1003	9.36 ± 0.37	8.00	0.0672	3
5	1750	17.51 ± 1.83	16.52	0.4886	9.85 ± 1.90	9.372	0.7385	3
5	2000	18.67 ± 1.94	17.24	0.1298	10.97 ± 1.01	10.90	0.8675	6
10	1000	14.79 ± 0.89	14.51	0.6810	8.19 ± 0.48	7.26	0.0563	3
10	1250	15.24 ± 0.50	15.56	0.4475	8.57 ± 0.53	7.60	0.0605	3
10	1500	17.49 ± 1.15	16.55	0.3144	10.90 ± 0.39	10.90	0.0565	3
10	1750	17.72 ± 0.35	17.25	0.1117	11.28 ± 0.36	10.86	0.1502	3
10	2000	18.85 ± 0.14	18.09	0.0390*	12.40 ± 0.26	12.64	0.5036	4
100	800	13.60 ± 0.98	15.47	0.0534	7.59 ± 0.74	7.68	0.8720	6
100	1000	16.15 ± 2.00	16.56	0.7604	10.92 ± 1.34	9.50	0.1482	4
100	1250	18.99 ± 0.33	17.78	0.0166*	12.27 ± 2.87	11.67	0.7990	5
100	1500	21.01 ± 3.13	18.84	0.2466	13.70 ± 0.80	13.77	0.8687	5

IV. CONCLUSION

In this study, the dynamic conductivity changes during H-FIRE treatment of 5 μs and 10 μs pulses were quantified and compared to conventional IRE pulses. The simulation results were in good agreement with the experimental results on in vivo rabbit livers. These included the current at the end of the first burst or pulse and the value of the electric field thresholds of ablation determined at the end of treatment. The coefficient A, which determines the differential change in conductivity caused by the electroporation-inducing pulses, was larger for the conventional IRE pulses than the H-FIRE bursts, indicating that conductivity changes are mitigated during H-FIRE treatment. While the study has been conducted for 90 H-FIRE bursts of 10 μs and 5 μs widths, the method developed can be easily adapted to different H-FIRE widths and numbers of bursts.

ACKNOWLEDGMENT

The authors would like to thank China Scholarship Council and the Institute for Critical Technology and Applied Science for their support of this research. They would also like to thank Dr. H. Wang and Dr. J. L. Robertson for their help in pathological analysis. R. V. Davalos has pending and accepted patents on IRE and H-FIRE.

REFERENCES

[1] L. M. Mir *et al.*, "Biomedical applications of electric pulses with special emphasis on antitumor electrochemotherapy," *Bioelectrochem. Bioenergetics*, vol. 38, no. 1, pp. 203–207, 1995.
[2] M. J. Jaroszeski *et al.*, "Electrochemotherapy: An emerging drug delivery method for the treatment of cancer," *Adv. Drug Del. Rev.*, vol. 26, no. 2, pp. 185–197, 1997.
[3] L. M. Mir, "Therapeutic perspectives of in vivo cell electropermeabilization," *Bioelectrochemistry*, vol. 53, no. 1, pp. 1–10, 2001.
[4] R. Heller *et al.*, "Treatment of B16 mouse melanoma with the combination of electropermeabilization and chemotherapy," *Bioelectrochem. Bioenergetics*, vol. 36, no. 1, pp. 83–87, 1995.
[5] R. V. Davalos, "Real-time imaging for molecular medicine through electrical impedance tomography of electroporation," Ph.D. dissertation, Dept. Mech. Eng., Univ. California, Berkeley, CA, USA, 2002.
[6] C. Yao *et al.*, "Experimental studies on killing and inhibiting effects of steep pulsed electric field (SPEF) to target cancer cell and solid tumor," *IEEE Trans. Plasma Sci.*, vol. 32, no. 4, pp. 1626–1633, Aug. 2004.
[7] R. V. Davalos *et al.*, "Tissue ablation with irreversible electroporation," *Ann. Biomed. Eng.*, vol. 33, no. 2, pp. 223–231, 2005.
[8] L. Miller *et al.*, "Cancer cells ablation with irreversible electroporation," *Technol. Cancer Res. Treat.*, vol. 4, no. 6, pp. 699–705, 2005.
[9] B. Al-Sakere *et al.*, "Tumor ablation with irreversible electroporation," *Plos One*, vol. 2, no. 11, p. e1135, 2007.
[10] J. C. Weaver and Y. A. Chizmadzhev, "Theory of electroporation: A review," *Bioelectrochem. Bioenergetics*, vol. 41, no. 2, pp. 135–160, 1996.
[11] S. N. Goldberg *et al.*, "Thermal ablation therapy for focal malignancy: A unified approach to underlying principles, techniques, and diagnostic imaging guidance," *Amer. J. Roentgenol.*, vol. 174, no. 2, pp. 323–331, 2000.
[12] J. Zeng *et al.*, "The safety and efficacy of irreversible electroporation for large hepatocellular carcinoma," *Technol. Cancer Res. Treat.*, vol. 16, no. 1, pp. 120–124, 2017.
[13] R. C. Martin *et al.*, "Intra-operative anesthesia management in patients undergoing surgical irreversible electroporation of the pancreas, liver, kidney, and retroperitoneal tumors," *Anesthesiol. Pain Med.*, vol. 5, no. 2, p. e22786, 2015.
[14] R. C. G. Martin *et al.*, "Efficacy of preoperative immunonutrition in locally advanced pancreatic cancer undergoing irreversible electroporation (IRE)," *Eur. J. Surg. Oncol.*, vol. 43, no. 4, pp. 772–779, 2017.
[15] L. Bond *et al.*, "Intra-operative navigation of a 3-dimensional needle localization system for precision of irreversible electroporation needles in locally advanced pancreatic cancer," *Eur. J. Surg. Oncol.*, vol. 43, no. 2, pp. 337–343, 2017.
[16] E. M. Dunki-Jacobs *et al.*, "Evaluation of thermal injury to liver, pancreas and kidney during irreversible electroporation in an in vivo experimental model," *Brit. J. Surg.*, vol. 101, no. 9, pp. 1113–1121, 2014.
[17] S. P. Bhonsle *et al.*, "Characterization of irreversible electroporation ablation with a validated perfused organ model," *J. Vasc. Interventional Radiol.*, vol. 27, no. 12, pp. 1913–1922.e2, 2016.
[18] A. Golberg and M. L. Yarmush, "Nonthermal irreversible electroporation: Fundamentals, applications, and challenges," *IEEE Trans. Biomed. Eng.*, vol. 60, no. 3, pp. 707–714, Mar. 2013.
[19] M. B. Sano *et al.*, "Bursts of bipolar microsecond pulses inhibit tumor growth," *Sci. Rep.*, vol. 5, 2015, Art. no. 14999.
[20] C. B. Arena *et al.*, "High-frequency irreversible electroporation (H-FIRE) for non-thermal ablation without muscle contraction," *Biomed. Eng. Online*, vol. 10, no. 1, p. 102, 2011.
[21] S. P. Bhonsle *et al.*, "Mitigation of impedance changes due to electroporation therapy using bursts of high-frequency bipolar pulses," *Biomed. Eng. Online*, vol. 14, Suppl. 3, p. S3, 2015.
[22] C. B. Arena *et al.*, "Theoretical considerations of tissue electroporation with high-frequency bipolar pulses," *IEEE Trans. Biomed. Eng.*, vol. 58, no. 5, pp. 1474–1482, May 2011.

[23] C. Yao *et al.*, "Dielectric variations of potato induced by irreversible electroporation under different pulses based on the Cole-Cole model," *IEEE Trans. Dielectr. Electr. Insul.*, vol. 24, no. 4, pp. 2225–2233, Sep. 2017.
[24] I. A. Siddiqui *et al.*, "Induction of rapid, reproducible hepatic ablations using next-generation, high frequency irreversible electroporation (H-FIRE) in vivo," *HPB*, vol. 18, no. 9, pp. 726–734, 2016.
[25] C. Yao *et al.*, "Bipolar microsecond pulses and insulated needle electrodes for reducing muscle contractions during irreversible electroporation," *IEEE Trans. Biomed. Eng.*, vol. 64, no. 12, pp. 2924–2937, Dec. 2017.
[26] T. Miklovic *et al.*, "A comprehensive characterization of parameters affecting high-frequency irreversible electroporation lesions," *Ann. Biomed. Eng.*, vol. 45, pp. 2524–2534, Jul. 2017.
[27] D. Sel *et al.*, "Sequential finite element model of tissue electropermeabilization," *IEEE Trans. Biomed. Eng.*, vol. 52, no. 5, pp. 816–827, May 2005.
[28] J. F. Edd and R. V. Davalos, "Mathematical modeling of irreversible electroporation for treatment planning," *Technol. Cancer Res. Treat.*, vol. 6, no. 4, pp. 275–286, 2007.
[29] R. E. Neal *et al.*, "Experimental characterization and numerical modeling of tissue electrical conductivity during pulsed electric fields for irreversible electroporation treatment planning," *IEEE Trans. Biomed. Eng.*, vol. 59, no. 4, pp. 1076–1085, Apr. 2012.
[30] P. A. Garcia *et al.*, "Intracranial nonthermal irreversible electroporation: In vivo analysis," *J. Membrane Biol.*, vol. 236, no. 1, pp. 127–136, 2010.
[31] S. Gabriel, "The dielectric properties of biological tissues: III. Parametric models for the dielectric spectrum of tissues," *Phys. Med. Biol.*, vol. 41, pp. 2271–2293, 1996.
[32] D. Haemmerich *et al.*, "In vivo electrical conductivity of hepatic tumours," *Physiol. Meas.*, vol. 24, no. 2, p. 251, 2003.
[33] I. Lackovi *et al.*, "Incorporating electroporation-related conductivity changes into models for the calculation of the electric field distribution in tissue," in *Proceedings of IFMBE (XII Mediterranean Conference on Medical and Biological Engineering and Computing)*, R. Magjarevic, Ed. Berlin, Germany: Springer, 2010, pp. 695–698.
[34] S. Corovic *et al.*, "Modeling of electric field distribution in tissues during electroporation," *Biomed. Eng. Online*, vol. 12, no. 1, p. 16, 2013.
[35] R. E. Neal *et al.*, "A study using irreversible electroporation to treat large, irregular tumors in a canine patient," in *Proc. 2010 Annu. Int. Conf. IEEE Eng. Med. Biol. Soc.*, Aug. 2010, pp. 2747–2750.
[36] F. A. Duck, *Physical Properties of Tissues: A Comprehensive Reference Book*. San Diego, CA, USA: Academic, 1990.
[37] B. L. Ibey *et al.*, "Bipolar nanosecond electric pulses are less efficient at electropermeabilization and killing cells than monopolar pulses," *Biochem. Biophys. Res. Commun.*, vol. 443, no. 2, pp. 568–573, 2014.
[38] D. C. Sweeney *et al.*, "Quantification of cell membrane permeability induced by monopolar and high-frequency bipolar bursts of electrical pulses," *Biochimica et Biophysica Acta, Biomembranes*, vol. 1858, no. 11, pp. 2689–2698, 2016.
[39] M. Bonakda *et al.*, "The feasibility of a smart surgical probe for verification of IRE treatments using electrical impedance spectroscopy," *IEEE Trans. Biomed. Eng.*, vol. 62, no. 11, pp. 2674–2684, Nov. 2015.
[40] J. Langus *et al.*, "Dynamic finite-element model for efficient modelling of electric currents in electroporated tissue," *Sci. Rep.*, vol. 6, 2016, Art. no. 26409.